RESEARCH

Open Access

Analysis of Short-Term Prestress Losses in Post-tensioned Structures Using Smart Strands

Sang-Hyun Kim[1], Sung Yong Park[2], Sung Tae Kim[2] and Se-Jin Jeon[3*]

Abstract

The proper estimation of prestressing force (PF) distribution is critical to ensure the safety and serviceability of prestressed concrete (PSC) structures. Although the PF distribution can be theoretically calculated based on certain predictive equations, the resulting accuracy of the theoretical PF needs to be further validated by comparison with reliable test data. Therefore, a Smart Strand with fiber optic sensors embedded in a core wire was developed and applied to a full-scale specimen and two long-span PSC girder bridges in this study. The variation in PF distribution during tensioning and anchoring was measured using the Smart Strand and was analyzed by comparison with the theoretical distribution calculated using the predictive equations for short-term prestress losses. In particular, the provisions for anchorage seating loss and elastic shortening loss were reviewed and possible improvements were proposed. A new method to estimate the amount of anchorage slip based on real PF distributions revealed that the general assumption of 3–6-mm slip falls within a reasonable range. Finally, the sensitivity of the PF distribution to a few of the variables included in the equation of the elastic shortening loss was examined. The study results confirmed that the developed Smart Strand can be used to improve the design parameters or equations in PSC structures by overcoming the drawbacks of conventional sensing technologies.

Keywords: prestressed concrete, prestressing tendon, strand, prestressing force, prestress loss, fiber optic sensor, fiber Bragg grating

1 Introduction

The correct level of the prestress introduced by prestressing tendons, such as seven-wire strands, is critical to ensure the safety and serviceability of prestressed concrete (PSC) structures. The prestressing force (PF) distribution is usually estimated based on certain predictive equations specified in design codes and specifications. However, the frequently reported deterioration of PSC structures, including cracks and abnormal deformation, has been largely attributed to inappropriate theoretical

estimation of PF distribution. Short- and long-term prestress losses (Nilson, 1987) have a crucial effect on the spatial and time-dependent distribution of the PF. Therefore, the theoretical prestress losses should be verified by comparison with reliable data obtained from test specimens or, more preferably, from real-scale structures. Although this has been achieved using conventional sensors or techniques, these previous studies were incapable of validating the accuracy of the existing equations for predicting prestress losses.

For instance, electrical resistance strain gauges (ERSGs) that have been frequently used to measure the strains of structural components could not be applied successful to prestressing tendons. When attached to the surface of the helical wires of a seven-wire strand, the ERSGs were prone to damage during tensioning of the strands

*Correspondence: conc@ajou.ac.kr
[3] Department of Civil Systems Engineering, Ajou University, 206, Worldcup-ro, Yeongtong-gu, Suwon-si 16499, Gyeonggi-do, Korea
Full list of author information is available at the end of the article

Kim *et al. Int J Concr Struct Mater*   (2022) 16:1

Page 2 of 15

in post-tensioned members and releasing of the strands in pretensioned members, resulting in unreliable data. Other experimental approaches also showed some limitations in comprehensibly predicting the PF distribution required for validating the prestress losses. Some studies indirectly derived the strand strains from the measurement of concrete strains (Abdel-Jaber & Glisic, 2019; Garber et al., 2015), resulting in less accurate and limited information on the strains of a strand. In some other studies, the strand strain could be obtained only at the anchorage of a tendon using load cells (Burns et al., 1991) or lift-off test (Lundqvist & Nilsson, 2011). The complete distribution of PF along a tendon, as affected by prestress losses, could not be obtained by the conventional sensing technologies adopted in these previous studies. Furthermore, even more recent and advanced technologies could not completely overcome these drawbacks in terms of PF distribution: several examples are ultrasonic waves (Washer et al., 2002), vibration analysis (Kim et al., 2004), elasto-magnetic sensors (Cho et al., 2015), and acoustic emission (Chaki & Bourse, 2009).

Fiber optic sensors have also been used due to their relatively improved accuracy and durability compared to other sensors (Yao et al., 2021). Among several types of fiber optic sensors, fiber Bragg grating (FBG) has been preferred because of its well-established theoretical background and its strong validation based on accumulated experience and data (Majumder et al., 2008; Rodrigues et al., 2010). However, attachment of the fiber optic sensor to the strand surface (Gao et al., 2006; Perry et al., 2014; Shen et al., 2018) causes potential problems similar to those of ERSGs exposed to damage and, therefore, does not take full advantage of fiber optic sensors.

Therefore, the Smart Strand with the fiber optic sensors embedded in a core wire was developed in this study to estimate the PF distribution while overcoming these limitations and drawbacks of conventional sensing technologies. The developed Smart Strand was used to measure and analyze the variation in PF distribution during tensioning and anchoring by comparison with the theoretical distribution calculated using the predictive equations for short-term prestress losses. In particular, the provisions for anchorage seating loss and elastic shortening loss were reviewed and possible improvements were proposed. Although the prestress losses were experimentally investigated using the fiber optic sensors in previous studies (Yao et al., 2021), they focused on the varying trend of the PF distribution affected by prestress losses, not on the mutual validation of the measured data and the existing theoretical equations related to the prestress losses. Furthermore, this study adopted two actual PSC girder bridges with a span of as long as 60 m and a 20-m-long full-scale specimen to investigate the prestress losses more realistically, extending the applicability of fiber optic sensors over the small-to-medium-scale specimens mainly considered in previous studies (Yao et al., 2021). The study results confirm that the developed Smart Strand can be used to verify and improve the design equations in PSC structures.

2 Configuration of the Smart Strand
The characteristics of the Smart Strand are briefly introduced herein, although more detailed information can be found in some previous studies (Kim et al., 2015, 2020). Fig. 1 shows the shape and dimensions of a Smart Strand, which are almost identical to those of

Fig. 1 Shape and dimensions of a Smart Strand: **a** Section A–A and dimensions; **b** overall shape.
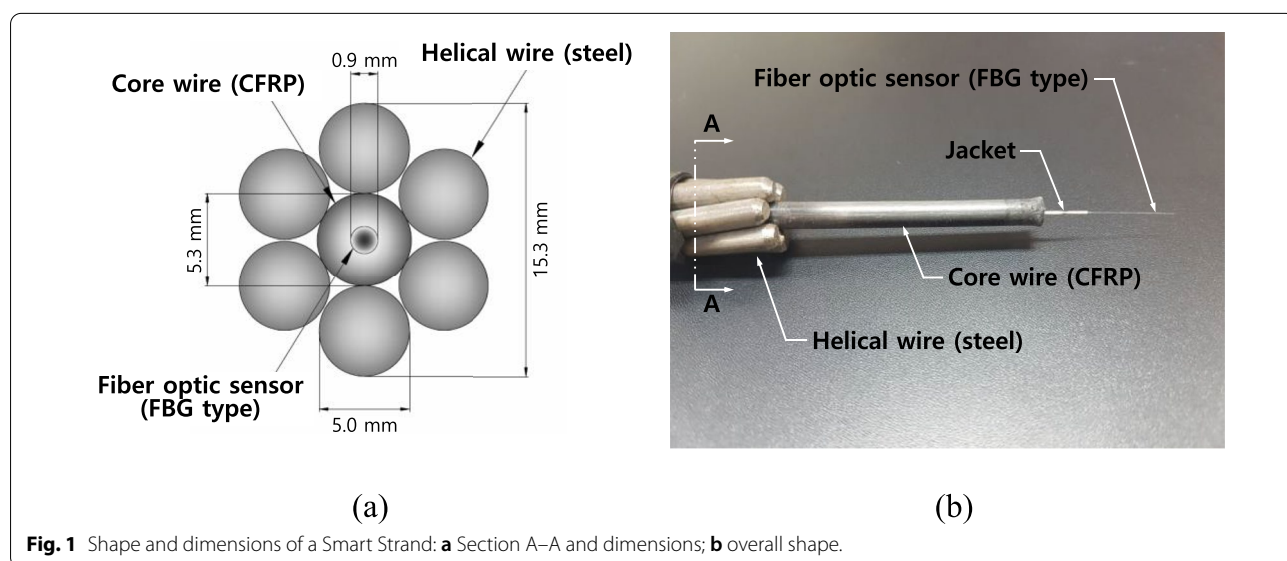
a standard seven-wire strand of Grade 1860 (ultimate tensile strength $f_{pu}=1860$ MPa) with a diameter of 15.24 mm (ASTM, 2018). The apparent feature of the Smart Strand is the replacement of the steel core wire in a regular strand with carbon fiber reinforced polymer (CFRP) core wire to accommodate the embedment of the fiber optic sensor with FBGs. The cross section of the fiber includes a core, a cladding, and coatings (Yao et al., 2021). Although the difference in strains between the core and the coatings was investigated previously (Tan et al., 2021), this strain transfer effect was not considered in this study, because a quantitative measure of the effect was not fully established yet.

Because the stress–strain relation of the Smart Strand is similar to that of a regular strand, the Smart Strand can be regarded as both a sensor and a structural component. The accumulated experience on the Smart Strand (Jeon et al., 2015, 2019; Kim et al., 2019, 2020) ensured the accurate and stable measurement of the short- and long-term strains of the strand, mainly due to the durability of the sensor surrounded and protected by CFRP, and further to the specific advantages of the fiber optic sensor and FBG. Moreover, the Smart Strand can also be used to directly measure the true axial strain of a strand when compared to the slightly sloped strain with respect to the axial axis obtained by a sensor attached on the surface of a helical wire. Attempts to embed the FBG into the core wire of a strand have been previously reported (Kim et al., 2012; Lan et al., 2014; Nellen et al., 1999). However, the Smart Strand developed in this study was validated by more cases than in other studies by taking field measurements of real structures and full-scale specimens.

Among various applications of the developed Smart Strand, the effect of long-term prestress losses on PF distribution was previously investigated (Kim et al., 2020). In addition, the friction coefficients related to the friction loss in short-term prestress losses were investigated previously (Jeon et al., 2015; Kim et al., 2019). However, anchorage seating loss and elastic shortening loss in the short-term prestress losses have not yet been studied in detail using the Smart Strand; therefore, this study was formulated to fill this research gap.

As a basic principle of FBG, the change of the wavelength of a light wave that is reflected at each FBG can be converted to strain by Eq. (1). The effect of the change of ambient temperature on the strain is excluded in Eq. (1), because this study only deals with short-term measurement. The extended form of Eq. (1) that includes the temperature compensation required for long-term measurement is presented in a reference (Kim et al., 2020):

$$\varepsilon = \frac{1}{1-p_e} \cdot \frac{\Delta\lambda}{\lambda_B}, \tag{1}$$

where ε is the strain, p_e is the photo-elastic coefficient ($=0.22$), $\Delta\lambda = \lambda - \lambda_B$ is the wavelength shift, λ is the measured wavelength, and λ_B is the base wavelength at the start of measurement. The strain obtained in Eq. (1) can be converted to PF using the linear force–strain relation shown in Eq. (2), which is valid over the practical range expected in the service of PSC structures:

$$P = (E_p A_p)_{\text{smart}} \varepsilon_p, \tag{2}$$

where P is the PF at an FBG, $(E_p A_p)_{\text{smart}}$ is the equivalent $E_p A_p$ of a Smart Strand ($=26{,}600$ kN), E_p is the modulus of elasticity of a strand, A_p is the cross-sectional area of a strand, and ε_p is the strain measured at an FBG of a Smart Strand which corresponds to ε in Eq. (1). Because the Smart Strand is a hybrid material of steel and CFRP, the value of $(E_p A_p)_{\text{smart}}$ was experimentally obtained through the tensile test of the Smart Strand.

3 Short-Term Losses of Prestress

Fig. 2 shows the sources of prestress losses that can occur in the short and long terms and the corresponding PF affected by these losses. The short-term losses, which are

Fig. 2 Short- and long-term prestress losses.
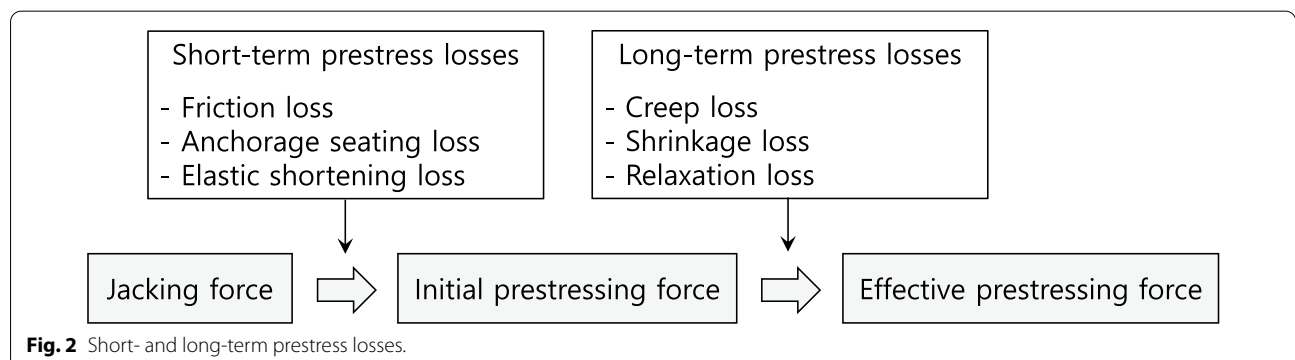
also called instantaneous losses or immediate losses, are the main focus of this study. The long-term losses or time-dependent losses were previously analyzed using the same specimen and actual structures as those of this study (Kim et al., 2020). The previous study reported that the developed Smart Strands are useful for the measurement of the long-term PF distribution.

Friction loss occurs due to the contact between strands and a duct during tensioning, where curvature friction is induced at the curved part of a duct, whereas wobble friction is caused at the unintendedly deformed part of a duct. The reduction of PF as affected by the friction can be formulated by Eq. (3) with two types of friction coefficients (Nilson, 1987):

$$P_x = P_j e^{-(\mu\alpha+kl)} \approx P_j[1 - (\mu\alpha + kl)], \quad (3)$$

where P_x is the PF at the distance x along a tendon from the jacking point, P_j is the jacking force, μ is the curvature friction coefficient, k is the wobble friction coefficient, α is the variation of angle, and l is the distance. The exponential function can be approximated as a linear function, as also shown in Eq. (3) when $\mu\alpha + kl$ is sufficiently small, e.g., $\mu\alpha + kl \leq 0.3$. In previous studies (Jeon et al., 2015; Kim et al., 2019), the range of reasonable friction coefficients was derived from the newly proposed methodologies in combination with the data measured using the developed Smart Strands.

Anchorage seating (also called anchorage slip or anchorage set) loss inevitably occurs as the wedges seat themselves into the strands and an anchor head upon release of the jacking force. This draw-in slip ranges from 3 to 6 mm depending on various factors (Nilson, 1987). Given that the slip is also affected by the friction between the strands and a duct, the slip is mostly confined to a region close to the live end, i.e., the jacking anchorage, and the PF distribution is symmetrized due to the reverse friction at this region. These assumptions are depicted in Fig. 3, from which Eqs. (4)–(6) can be derived (Joint ACI-ASCE Committee 423, 2016). The slope indicated by p can be assumed linear based on a simplification of Eq. (3):

$$l_{set} = \sqrt{\frac{E_p A_p \Delta l}{p}}, \quad (4)$$

$$\Delta P = 2pl_{set}, \quad (5)$$

$$\Delta l = \frac{(\text{area of triangle})}{E_p A_p} = \frac{\Delta P l_{set}}{2E_p A_p}, \quad (6)$$

where l_{set} is the distance affected by anchorage seating, E_p is the modulus of elasticity of strands, A_p is the
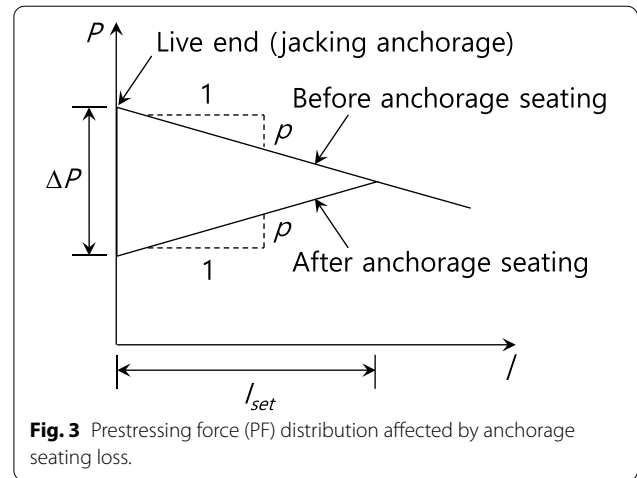

Fig. 3 Prestressing force (PF) distribution affected by anchorage seating loss.

cross-sectional area of strands, Δl is the draw-in slip displacement, p is the friction loss of PF per unit length, and ΔP is the anchorage seating loss of PF at the live end. Note that Δl can be expressed as a function of the area of the triangle enclosed by the PFs before and after the anchorage seating in Eq. (6).

Elastic shortening loss is induced, because the prestressing tendons are also shortened when a PSC member is subjected to compression induced by prestressing. In the case of a post-tensioned member, a group of strands are sequentially tensioned duct-by-duct using a multi-strand jack. Therefore, the PF of a prestressing tendon that is previously tensioned and anchored is affected by the subsequent tensioning operation of the other remaining tendons. Although an average value of the elastic shortening loss of all the tendons is generally used for the design purpose (Joint ACI-ASCE Committee 423, 2016), the elastic shortening loss of a specific Smart Strand can also be considered in Eqs. (7) and (8). That is, e_{sm} is used instead of e_p, because the value measured at a Smart Strand is compared with the theoretical value predicted by Eq. (8). The elastic shortening loss of Eq. (8) is based on the assumption of composite action between concrete and a strand:

$$f_{ci} = \left(\frac{P_i}{A_c} + \frac{P_i e_p}{I_c}e_{sm}\right) - \frac{M_d}{I_c}e_{sm}, \quad (7)$$

$$\Delta f_{pES} = nf_{ci}, \quad (8)$$

where f_{ci} is the compressive stress of concrete caused by prestressing and self-weight at the location of the strand in concern, P_i is the total initial PF of all the subsequent strands that are tensioned after the strand in concern, A_c is the area of the concrete section, I_c is the second moment of area of the concrete section, e_p is the average eccentricity of all the subsequent strands, which are

Kim *et al. Int J Concr Struct Mater*   (2022) 16:1

Page 5 of 15

tensioned after the strand in concern, with respect to the concrete centroid, e_{sm} is the eccentricity of the strand in concern (a Smart Strand in this study) of which the stress needs to be obtained, M_d is the bending moment due to self-weight with the unit weight of PSC as 25 kN/m^3, which is activated by the camber deformation during tensioning, Δf_{pES} is the elastic shortening loss in stress, n is the modular ratio ($= E_p/E_c$), E_p is the modulus of elasticity of strand, and E_c is the modulus of elasticity of concrete. Although an iterative procedure is required to accurately account for P_i, it is usually adequate to estimate $P_i \approx 0.9P_j$, where P_j is the jacking force (Nilson, 1987).

4 Experimental Program of Prestressed Concrete (PSC) Structures

4.1 Post-tensioned Full-Scale Specimen
A 20-m-long full-scale post-tensioned specimen was fabricated to investigate the short- and long-term characteristics of PF using Smart Strands, as shown in Fig. 4. Three ducts with different curvatures were arranged as denoted by T1, T2, and T3 in Fig. 4. Twelve 15.2-mm-diameter strands, with ultimate tensile strength (f_{pu}) of 1860 MPa, were inserted into an 85-mm-diameter galvanized metal duct and tensioned up to $0.7f_{pu}$ at one end of the specimen using a multi-strand jack, in the order of T1, T2, and T3, when the concrete compressive strength reached 30 MPa with the mix proportion shown in Table 1. The Smart Strands were selectively inserted into each duct together with regular strands as shown in the anchor heads of Fig. 5 with the identification of each hole. Three

types of Smart Strands were fabricated with three, five, and seven FBGs, respectively, which are indicated as a number in the Smart Strand in Fig. 5. Five and seven FBGs were equally spaced along a Smart Strand with the margin of 1 m at both ends, whereas three FBGs were located at 1, 10, and 16 m from the jacking end.

4.2 Post-tensioned PSC Girder Bridges
To extend the applicability of Smart Strands to real infrastructures, two different types of post-tensioned PSC girder bridges (bridges A and B) were employed. Both bridges have eight 60-m-long girders, but their specified concrete compressive strengths are 60 MPa and 80 MPa in bridges A and B, respectively. These strengths were used for the theoretical calculation of elastic shortening loss, because tensioning was performed after a sufficient duration to attain them. Figs. 6 and 7 show the main dimensions and configuration of the galvanized metal ducts in A and B's girder, respectively. All the strands used in these girders have 15.2-mm diameter and $f_{pu} = 1860$ MPa.

Total four Smart Strands were fabricated with seven FBGs. Two different girders (girders 1 and 2) were chosen in each bridge and one Smart Strand was assigned to each girder. As also shown in Figs. 6 and 7, one Smart Strand has equally spaced FBGs, whereas the remaining three Smart Strands have the FBGs at the center and mainly near both ends to investigate the effect of anchorage slip on the PF distribution. The Smart Strands were inserted into the uppermost duct in the girder, where a larger friction loss would be
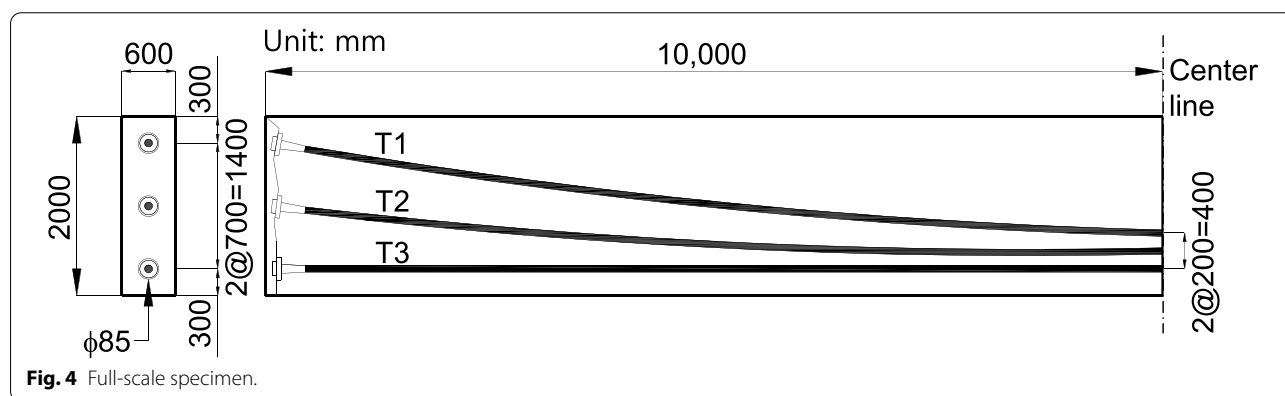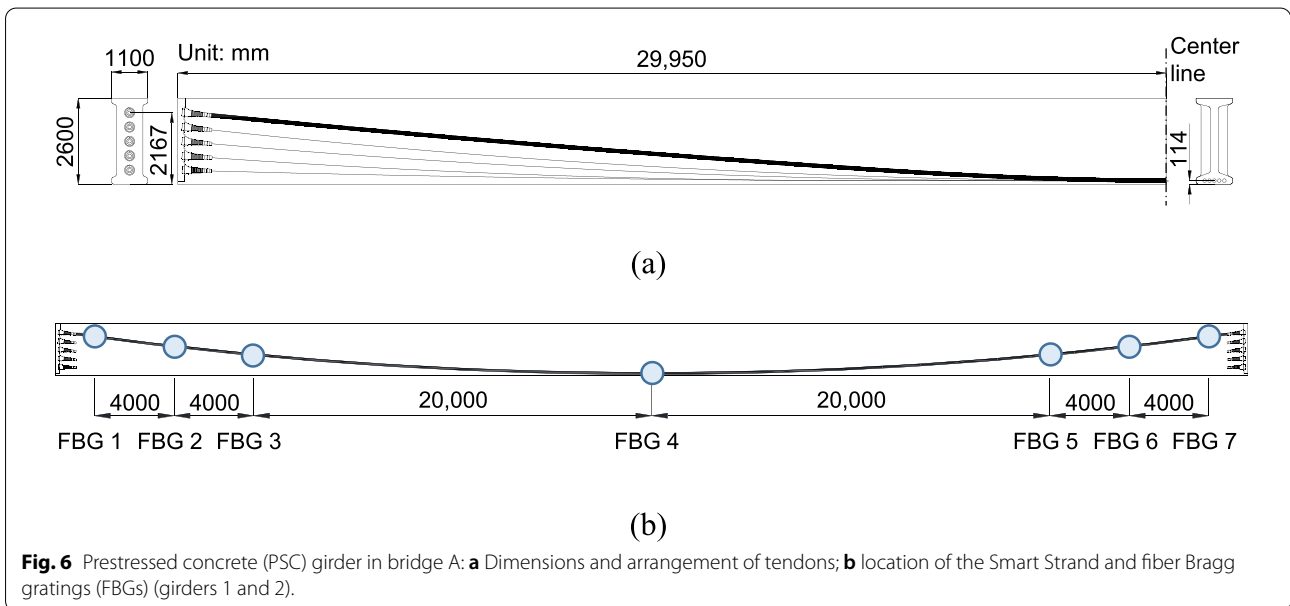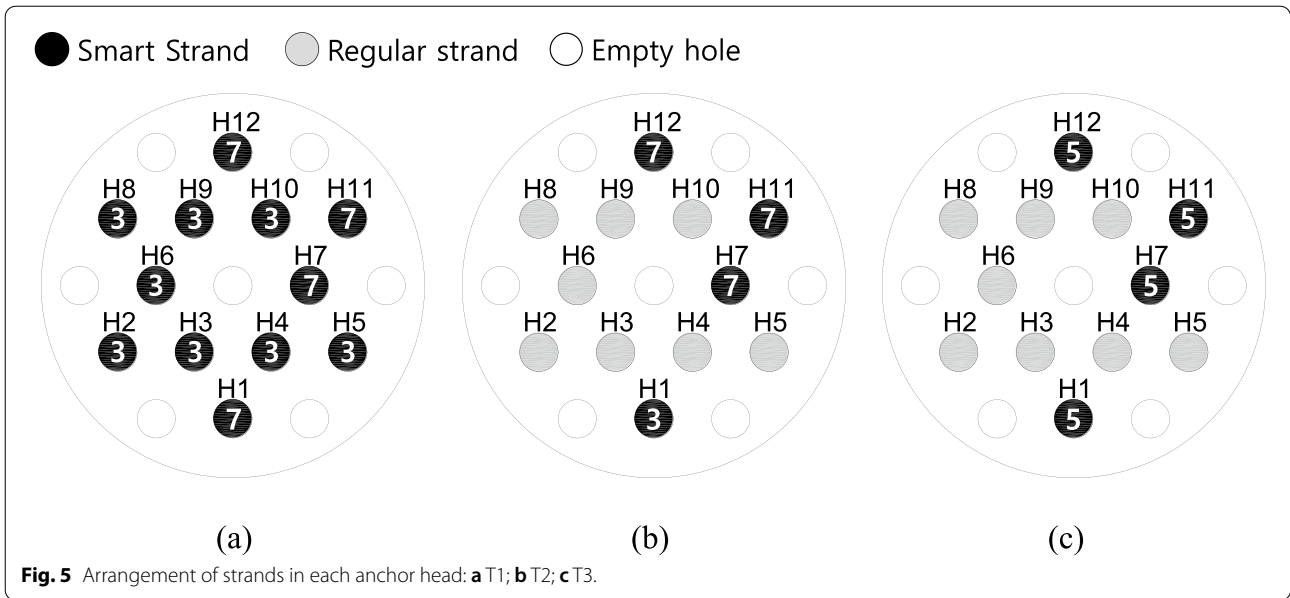

Fig. 4 Full-scale specimen.

Table 1 Mix proportion of full-scale specimen.

Water	Cement	Blast furnace slag	Fly ash	Fine aggregate	Coarse aggregate	High-range water reducing agent
160	376	47	47	798	909	5.64

Unit: kg/m^3.

Fig. 5 Arrangement of strands in each anchor head: **a** T1; **b** T2; **c** T3.

Fig. 6 Prestressed concrete (PSC) girder in bridge A: **a** Dimensions and arrangement of tendons; **b** location of the Smart Strand and fiber Bragg gratings (FBGs) (girders 1 and 2).

induced by the larger curvature than that of the other ducts. The Smart Strand was added to the original regular strands, which numbered 21 and 11, and the inner diameters of the corresponding ducts were 105 and 75 mm for bridges A and B, respectively. The strands in each duct were tensioned at both ends using two multi-strand jacks in both bridges, where the Smart Strand was tensioned approximately up to $0.67f_{pu}$. The Smart Strand experienced the elastic shortening loss

caused by all the strands included in the other ducts, because the uppermost duct with the Smart Strand was tensioned first in both bridges.

5 Prestressing Force (PF) Distribution During Tensioning and Anchoring

5.1 Post-tensioned Full-Scale Specimen

The PF distributions as affected by short-term prestress losses were represented for the Smart Strand T1–H7 (see
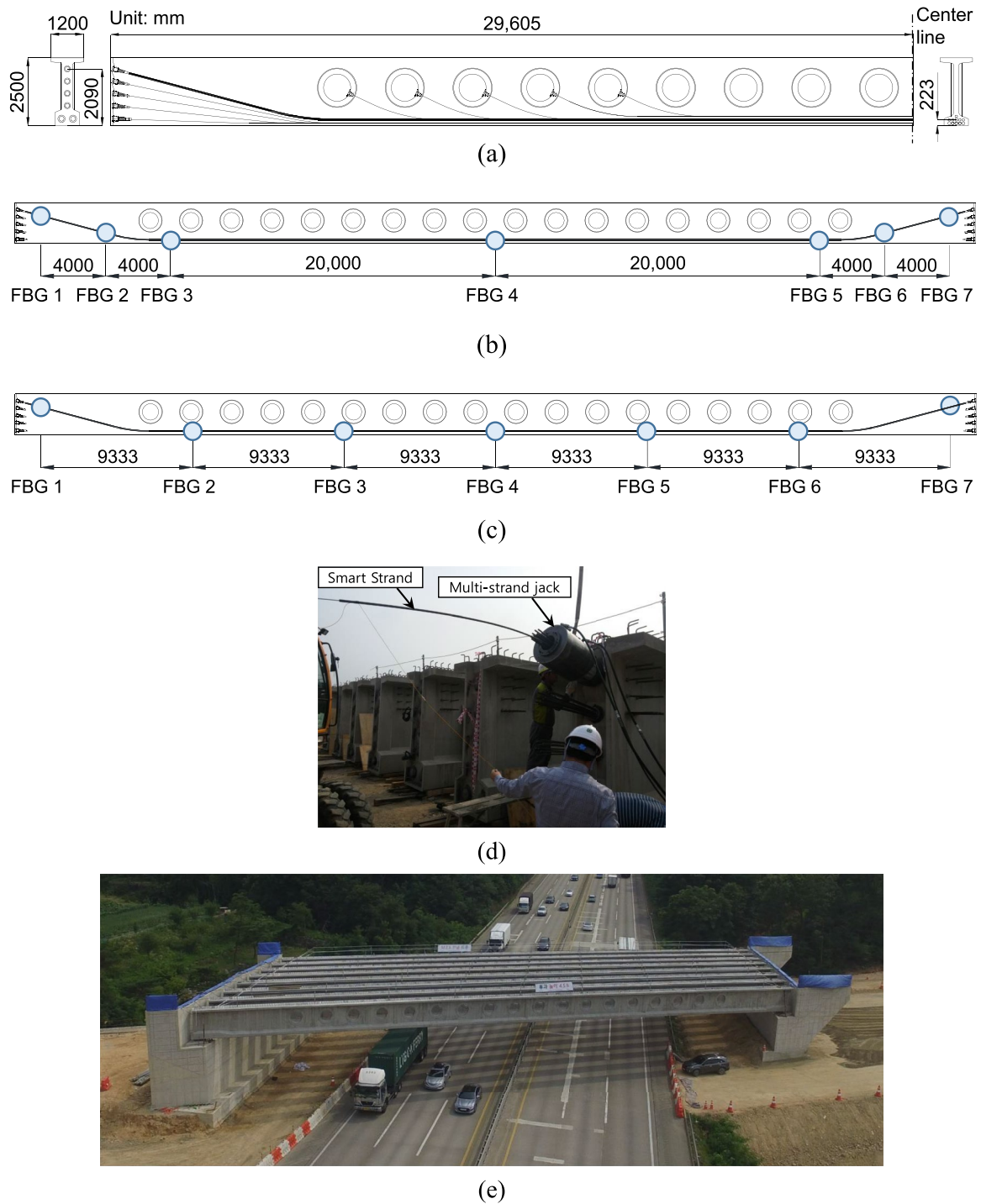
Fig. 7 PSC girder in bridge B: **a** Dimensions and arrangement of tendons; **b** location of the Smart Strand and FBGs (girder 1); **c** location of the Smart Strand and FBGs (girder 2); **d** tensioning of strands; **e** erected girders before placement of deck.

Figs. 4 and 5 for the location) in Table 2 and Fig. 8. The PF distribution was obtained by connecting the PF values measured at each FBG that correspond to the markers in Fig. 8, where the strands were tensioned at the left end.

The PF of a strand can vary slightly from strand-to-strand even in a duct due to the different degree of interlocking and slip at a hole of the anchor head. This aspect was analyzed by Cho et al. (2015) using elasto-magnetic sensors.

Table 2 PFs at the location of each FBG in full-scale specimen (T1–H7).

Distance (m)	1	4	7	10	13	16	19
After tensioning (kN)	171	171	164	163	163	159	157
After anchoring the strands in T1 (kN)	154	153	155	158	163	159	157
After anchoring the strands in T2 (kN)	152	150	151	154	161	157	155
After anchoring the strands in T3 (kN)	151	149	149	151	158	155	154

Fig. 8 PF distribution in full-scale specimen (T1–H7).

Fig. 9 PF distribution in girder 1 of bridge A.
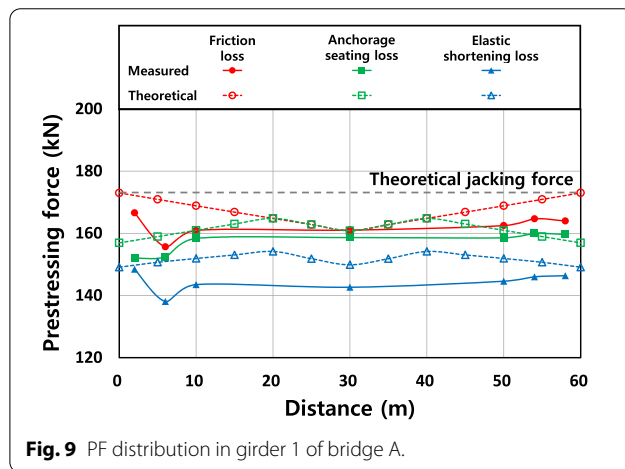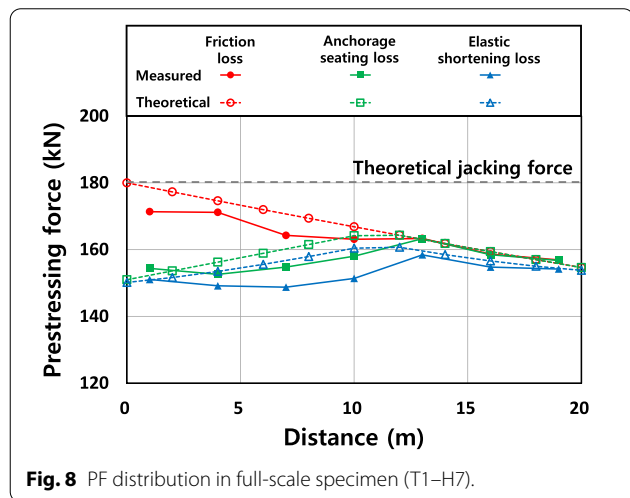
This explains why the PF of T1–H7 did not attain 180 kN, which corresponds to $0.7f_{pu}$, as initially intended after tensioning even at the left jacking end.

Fig. 8 apparently shows how the PF distributions are affected by each short-term prestress loss. The PF gradually decreases from the left end to the right end due to the friction loss during tensioning. However, this decreasing trend does not match the linear decrease resulting from the theoretical mathematical formula of Eq. (3), possibly due to the unexpected local wobble of a duct and inevitable entanglement of some strands while inserting into a duct and jacking. Then, the PF distribution near the anchorage zone decreases due to the anchorage seating loss, as depicted in Fig. 3. The PF distribution further decreases according to subsequent tensioning of the remaining strands included in the other ducts, in the order of T2 and T3.

The measured PF distributions were also compared with those theoretically estimated by Eqs. (3)–(8) at 2-m intervals in Fig. 8. The friction coefficients used for the theoretical PF distribution, which were derived from the previously proposed methodologies (Jeon et al., 2015; Kim et al., 2019), are $\mu = 0.21$/rad and $k = 0.0034$/m. For a more reasonable comparison, these friction coefficients based on the measured PF distribution were adopted instead of those provided in the existing provisions. With

an assumed anchorage slip of 6 mm, l_{set} in Fig. 3 was approximately 13 and 11 m in measurement and theory, respectively. The overall trend of PF distributions in each stage of short-term prestress losses was similar for the measured and theoretical values, although they showed some differences in absolute values. The final measured PF after short-term prestress losses was only 4.6% less than the theoretical value at mid-span. These results in Fig. 8 confirmed the usefulness of the existing predictive equations for the short-term prestress losses in estimating the PF distribution for design purposes.

5.2 Post-tensioned PSC Girder Bridges

Figs. 9 and 10 show the PF distributions of girder 1 in bridge A and girder 2 in bridge B, respectively, during the history of short-term prestress losses for both the measurement and theory. They were obtained based on the PF values at FBGs indicated by the markers in Figs. 9 and 10. The PF distributions of the measured data during tensioning, which correspond to the graphs for the friction loss in Figs. 9 and 10, do not exhibit a perfectly symmetrical shape, despite the tensioning at both ends, possibly for the reasons mentioned in Sect. 5.1. In particular, the PF distribution near the left end in Fig. 9 was very irregular. The friction coefficients used to produce theoretical PF distributions are: $\mu = 0.266$/rad and $k = 0.0015$/m
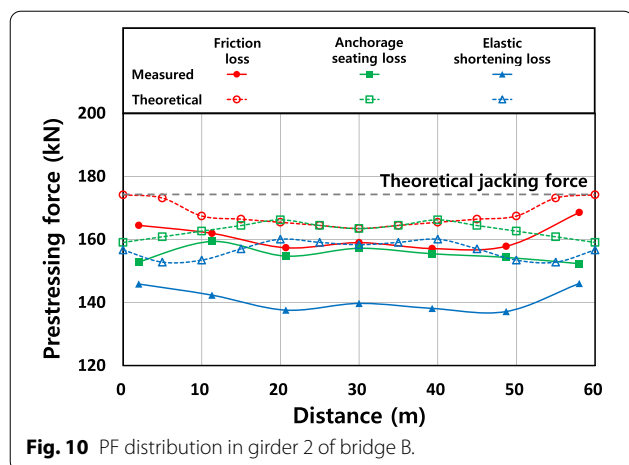
Fig. 10 PF distribution in girder 2 of bridge B.

in Fig. 9 and $\mu = 0.105$/rad and $k = 0.0012$/m in Fig. 10, which were also obtained based on previous studies (Jeon et al., 2015; Kim et al., 2019).

Even the theoretical PF distribution during tensioning in Fig. 10 does not show any linearity, which is explained as follows: in the parabolic shape of a tendon, the increase of α and l shown in Eq. (3) above is almost proportional to the horizontal distance along a member, which results in the linear PF distribution according to the assumption of Eq. (3), as evident in Figs. 8 and 9. However, the tendon profile of bridge B differs from the typical parabolic shape, as shown in Fig. 7, resulting in the nonlinear PF distribution in Fig. 10. This causes an inevitable discrepancy in estimating the anchorage slip loss, because the assumptions to draw Eqs. (4)–(6) are based on the linearity, as shown in Fig. 3. In this case, it is still recommended to apply the same equations for practical design purposes, using the averaged linear slope in the PF distribution during tensioning, as done in Fig. 10.

The anchorage slip was assumed to be 6 mm and the resulting l_{set} was approximately 20 m in both bridges. However, the trend of the measured anchorage slip differed from the idealized shape in Fig. 3 in that the slip was not limited to the end jacking regions but had an influence even on the mid-span, although the slip was mainly concentrated on the end regions. Furthermore, the PF distributions at the end regions before and after the anchorage seating did not exhibit a perfect mirror image with the reversed slopes, as shown in Fig. 3. This suggests that the actual PF distribution in real PSC structures can be more complicated than that realized in ideal conditions of test specimens.

The actual elastic shortening loss tended to be larger than the estimation in both bridges: 16.0 and 11.0 kN for measurement and theory, respectively, at the mid-span of bridge A, and 17.5 and 5.1 kN, respectively, at the

mid-span of bridge B. As a result, the measured final PFs after short-term losses were smaller than the theoretical ones in both bridges: the differences were 4.8 and 11.8% for bridges A and B, respectively. In Sect. 6.3, we will investigate whether the theoretical elastic shortening loss can be further adjusted to approach the measured value by applying more realistic values for the variables in Eqs. (7) and (8).

Despite these sources of differences, the design equations for the short-term prestress losses remain plausible for predicting the PF distribution in actual structures. However, the theoretical PF distribution was sensitive to the assumed values for the friction coefficients and slip displacement, which highlights the importance of reasonable design parameters. If the actual short-term PF differs greatly from the theoretical estimation, the concrete stresses can exceed the allowable stresses, possibly resulting in cracks, crushing, and abnormal camber or deflection. Therefore, it is desirable to ensure a sufficient margin in stresses when designing a PSC structure to account for such discrepancies.
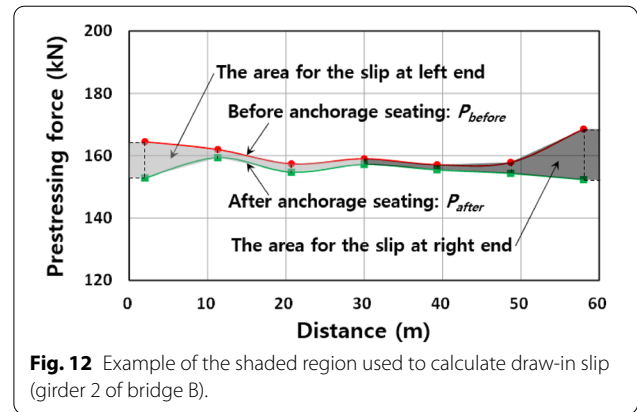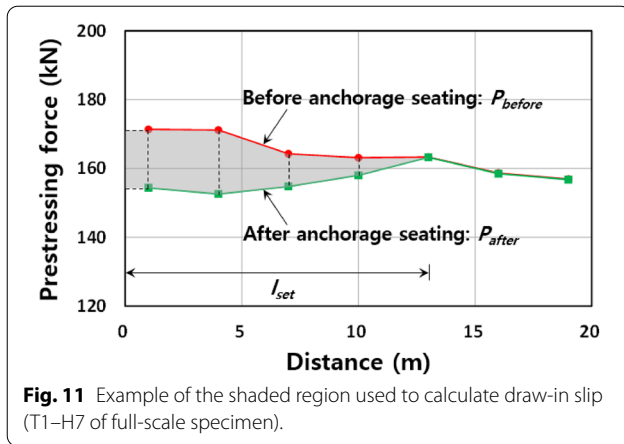
6 Additional Analysis of Short-Term Losses of Prestress

6.1 Friction Loss
As shown in Sect. 5, the friction loss occurs prior to other losses during tensioning and has a significant effect on the subsequent PF distributions. Although detailed analyses on the friction loss and methodologies to determine reasonable friction coefficients are beyond the scope of this study, they have been dealt with in previous studies (Jeon et al., 2015; Kim et al., 2019). The friction coefficients recommended in various provisions show a wide range of variation, e.g.: $\mu = 0.15 \sim 0.25$, $0.14 \sim 0.22$, and 0.19/rad; $k = 0.00066$, $0.0010 \sim 0.0023$, and $0.00095 \sim 0.0019$/m in AASHTO LRFD bridge design specifications (AASHTO, 2020), Post-tensioning manual (PTI, 2006), and Eurocode 2 (CEN, 2004), respectively. In this study, however, more realistic friction coefficients were obtained using the proposed methodologies of previous studies (Jeon et al., 2015; Kim et al., 2019) and applied to the analyses for a more reasonable comparison with the measured PF. As was noted in Sect. 5, the friction coefficients varied depending on the characteristics and conditions of each structure.

6.2 Anchorage Seating Loss
Although the amount of draw-in slip is usually assumed in the design by referring to the information provided by a manufacturer of the anchorage device, it strongly affects the PF distribution. For example, if the slip is increased from 3 to 6 mm, l_{set} and anchorage slip loss increase by as much as 41%, according to Eqs. (4) and

Fig. 11 Example of the shaded region used to calculate draw-in slip (T1–H7 of full-scale specimen).

Fig. 12 Example of the shaded region used to calculate draw-in slip (girder 2 of bridge B).

(5). Therefore, the manufacturer often suggests a conservatively large amount of slip of 6 mm, as evident in some relevant documents (VSL International Ltd., 2015). Therefore, the 6-mm slip was assumed in the calculations of the theoretical PF in Figs. 8, 9, and 10.

In this study, the PF distributions measured using the Smart Strands were utilized to validate the amount of slip. The principle underlying this procedure is that Eq. (6) can be applied to any shape, not only a triangle. That is, Eq. (6) can be extended to the form of Eq. (9), where Fig. 11 shows an example of the in-between shaded region for the PF distribution of T1–H7 in Fig. 8 that corresponds to the numerator of the following equation:

$$\Delta l = \frac{\int_0^{l_{set}} (P_{before} - P_{after})dl}{E_p A_p}, \tag{9}$$

where P_{before} and P_{after} indicate the PF before and after the anchorage seating, respectively, and all other notations have the same meanings as Eq. (6). The area of the shaded region, which can be idealized as a polygon, can be readily obtained by dividing the region into several sub-regions, as illustrated in Fig. 11, and summing up the area of each sub-region. The shape of the region which is not covered by the measurement of FBGs can be appropriately assumed referring to the overall shape.

On the other hand, when the strand is tensioned at both ends, only half the area with respect to mid-span is considered to calculate the slip occurring at each end. For example, Fig. 12 represents the shaded region for the PF distribution in girder 2 of bridge B shown in Fig. 10. The two curves do not meet at any point in this case as the slip affects overall length of the strand.

Tables 3 and 4 show the amount of slip estimated in each Smart Strand using the above-mentioned procedure in the full-scale specimen and bridges, respectively. In Table 3, only the Smart Strands with five or seven FBGs were used for the calculation, because those with three

Table 3 Draw-in slips at anchorages in full-scale specimen.

Duct	Smart Strand	Slip (mm)[a]
T1	H1	5.1
	H7	5.3
	H12	4.4
T2	H7	5.9
	H11	5.1
	H12	5.0
T3	H1	6.4
	H7	6.6
	H12	6.4

[a] Average: 5.6 mm, coefficient of variation: 13.0%.

Table 4 Draw-in slips at anchorages in bridges A and B.

Bridge	Girder	Anchorage	Slip (mm)[a]
A	1	Left end	4.7
		Right end	4.1
B	1	Left end	8.2
		Right end	5.2
	2	Left end	5.1
		Right end	6.2

[a] Average: 5.6 mm, coefficient of variation: 23.8%.

FBGs could not produce sufficiently accurate PF distribution to determine the slip (see Fig. 5). However, T1–H11 and T3–H11 were unavailable, because the entire PF distribution could not be obtained due to the damage in some FBGs. The anchorage slip in the strands of T3 affected the entire length due to the absence of curvature friction. The Smart Strand in girder 2 of bridge A was unavailable in Table 4, because it was damaged after tensioning.

The average draw-in slip was 5.6 mm both in the full-scale specimen and actual bridges, which validated the general assumption of 6 mm in slip. However, the

coefficient of variation that is defined by the standard deviation divided by average was much higher in the bridges than in the specimen, possibly because the full-scale specimen could be tested in more controlled and favorable circumstances than at a construction site of actual bridges. Tables 3 and 4 also suggest that the assumption of slip less than 4 mm is so unconservative that it may lead to overestimation of PF.

Finally, Eqs. (4) and (5) based on the assumption of the linear slope of the PF distributions affected by friction, as shown in Fig. 3, can be extended to consider the more realistic slope together with Eq. (9). However, this procedure would involve more complicated equations than Eqs. (4) and (5), and, therefore, is not recommended from a practical point of view.

6.3 Elastic Shortening Loss

The measured elastic shortening loss largely differed from the theoretical one in Figs. 8, 9, and 10. Therefore, we examined whether this discrepancy could be reduced by adopting certain strategies. The assumptions implied in Eqs. (7) and (8) are as follows. First, Eq. (8) assumes a perfect bond between the strand and surrounding concrete, because the modular ratio (n) is used based on strain compatibility. However, regardless of the subsequent grouting into the duct to realize bonded tendon, the tendon remains unbonded until all the tensioning operation is terminated. In the unbonded condition, the tendon strain does not coincide with the strain of the surrounding concrete but is averaged along the length of the tendon. Although this assumption is inevitable to derive a practical equation for elastic shortening loss, it may induce some errors. Second, although P_i is used in Eq. (7), P_i cannot be determined prior to the calculation of short-term losses. Therefore, $P_i \approx 0.9P_j$ is usually assumed to simplify the calculation. However, in reality, P_i does not maintain a constant value of $0.9P_j$ but varies along the span, as evident in Figs. 8, 9, and 10. This is another inevitable assumption that cannot easily be rectified. Third,

although a constant section was assumed in calculating M_d in Eq. (7), the section is usually gradually enlarged near the end region, as shown in Figs. 6 and 7, to accommodate anchorage devices and stress concentration at the end of post-tensioned structures. This would have minor effect on the distribution of M_d. Fourth, the gross section was used in the calculation of A_c, I_c, and M_d in Eq. (7). That is, it was assumed that the entire section is filled with concrete for convenience in calculation. In reality, however, the net section with the area of ducts deducted is a more accurate expression during tensioning and anchoring. On the other hand, although the concept of transformed section can also be used to account for the contribution of reinforcements, the effect on A_c and I_c would be negligible. Finally, the accuracy of E_c included in n of Eq. (8) can be an issue, because E_c varies widely.

In this study, we attempted to improve two of these aforementioned assumptions. First, the improvement made by adopting the net section is discussed. Table 5 compares the gross section with the net section, where the outer diameter of each corrugated duct was conservatively used to calculate the deducted area. In fact, consideration of the duct area affects all the variables included in Eq. (7). It also slightly changes the location of the centroidal axis along the member length, affecting e_p, e_{sm}, and I_c at each point, because the locations of ducts vary in longitudinal direction. However, the variables in Eq. (7) are not greatly affected by considering the net section, because the change in area only ranges from 1.6 to 5.3% in Table 5. Because the re-evaluation of e_p, e_{sm}, and I_c at every point in consideration involves cumbersome tasks, only the effect of change in A_c and M_d on the elastic shortening loss is analyzed. Table 6 shows the magnitude of the elastic shortening loss at mid-span in Figs. 8, 9, and 10 as affected by the deduction of duct area. The elastic shortening loss of the full-scale specimen was 6.7 kN for T1–H7 in Fig. 8. The elastic shortening loss of the twelve Smart Strands inserted into T1 ranged from 5.3 to 7.5 kN and averaged 6.2 kN. This revealed that the elastic

Table 5 Comparison of sectional area.

Structure	Area of gross section (mm^2) [1]	Duct			Area of net section (mm^2) [3] = [1]-[2]	Ratio (%) [3]/[1] × 100
		Outer diameter	Number	Total area (mm^2) [2]		
Full-scale specimen	1,200,000	89	3	18,663	1,181,337	98.4
Bridge A	1,157,000	106	5	44,124	1,112,876	96.2
Bridge B	966,000	89 [a]	2	50,745	915,255	94.7
		79 [a]	4			
		69 [b]	5			

[a] Primary prestressing anchored at ends.

[b] Secondary prestressing anchored at holes of web.

Table 6 Change in elastic shortening loss at mid-span according to sectional area.

Structure	Measurement (kN)	Theory (kN)		Ratio (%) [2]/[1] × 100
		Gross section [1]	Net section [2]	
Full-scale specimen	6.7	3.7	3.8	102.7
Bridge A	16.0	11.0	11.7	106.4
Bridge B	17.5	5.1	6.0	117.6

Table 7 Comparison of the modulus of elasticity of concrete.

Provision	Formula[a]	Modulus of elasticity (MPa)		
		Full-scale specimen [ratio (%)]	Bridge A [ratio (%)]	Bridge B [ratio (%)]
KCI (2012)	$E_c = 0.077 m_c^{1.5} \sqrt[3]{f_{cu}}$ $= 8500 \sqrt[3]{f_{cu}}$ $f_{cu} = f_{ck} + \Delta f$	27,537 [100]	34,351 [100]	37,519 [100]
ACI 318 (2019)	$E_c = w_c^{1.5} 0.043 \sqrt{f_c'}$ $= 4700 \sqrt{f_c'}$	25,743 [93.5]	36,406 [106.0]	42,038 [112.0]
Eurocode 2 (CEN, 2004)	$E_c = 22,000 (f_{cm}/10)^{0.3}$ $f_{cm} = f_{ck} + 8$	32,837 [119.2]	39,100 [113.8]	42,244 [112.6]

[a] E_c in MPa, m_c and w_c: unit weight of concrete with 23 kN/m³ for normal-weight concrete, f_{cu} and f_{cm}: mean value of compressive strength, f_{ck} and f_c': specified compressive strength, $\Delta f = 4$ and 6 MPa for $f_{ck} \leq 40$ MPa and $f_{ck} \geq 60$ MPa, respectively, and linear interpolation for $40 < f_{ck} < 60$ MPa.

shortening loss increased by 2.7~17.6% and approached the measured values by employing the net section instead of the gross section in original calculation. Nevertheless, the difference between the measurement and theory did not greatly diminish and the measured elastic shortening loss was still much larger than theoretical one.

Second, the effect of the modulus of elasticity on the elastic shortening loss is investigated. When compared to E_p which is considered a constant value of 200,000 MPa in this study, E_c varies depending on various factors, including compressive strength, unit weight, and moisture condition of concrete, various properties and volumetric proportion of aggregate (ACI Committee 318, 2019; Mehta & Monteiro, 2006; Neville, 1996). Many provisions

provide the formula for E_c as a function of dominant factors, such as compressive strength and unit weight (ACI Committee 318, 2019; CEN, 2004; KCI, 2012). Table 7 presents the modulus of elasticity calculated according to some representative provisions, where the specified compressive strength included in the formula indicates the strength attained when tensioning. In the original calculation of this study, E_c was obtained from KCI (2012). The modulus of elasticity of the full-scale specimen ranged from 93.5 to 119.2% when the original E_c is considered 100%, whereas that of the bridges A and B ranged from 106.0 to 113.8%. As shown in Eq. (8), the modulus of elasticity of concrete is inversely proportional to the elastic shortening loss, resulting in Table 8. That is, using E_c based on other provisions increased the difference between the theoretical elastic shortening loss and the measured one in most cases. However, the theoretical values that can be adjusted by modifying E_c remained insignificant when compared to the measured elastic shortening loss.

Based on the above analyses, we concluded that accurate prediction of the elastic shortening loss is difficult, because almost all the variables included in the predictive equations are affected by the accuracy in calculation and provisions. Furthermore, the predictive equations are founded on several intrinsic assumptions. The amount of the elastic shortening loss can vary to some extent by applying some improvement or the alternatives to each variable. A combination of two or more strategies would increase the variability in the elastic shortening loss. However, it was difficult to determine which strategy is effective, because the difference from the measured elastic shortening loss remained large in this study and the

Table 8 Change in elastic shortening loss at mid-span according to the modulus of elasticity of concrete.

Structure	Measurement (kN)	Theory (kN)		
		KCI (2012)	ACI 318 (ACI Committee 318, 2019)	Eurocode 2 (CEN, 2004)
Full-scale specimen	6.7	3.7	4.0	3.1
Bridge A	16.0	11.0	10.4	9.7
Bridge B	17.5	5.1	4.6	4.5

Kim *et al. Int J Concr Struct Mater*   (2022) 16:1

Page 13 of 15

trends of the measured and theoretical PF distributions are arbitrarily dependent on a structure. Further study is required to accumulate more measurement data to clarify the tendency of elastic shortening loss.

7 Conclusions

The prestressing force (PF) distribution in a PSC structure is closely related to the short- and long-term prestress losses. Although some predictive equations have been used to estimate these prestress losses, these equations were not sufficiently validated by comparison with the measured PF distribution. Therefore, the Smart Strand with fiber optic sensors of FBG type was developed and was applied to a 20-m-long full-scale post-tensioned specimen and two 60-m-long post-tensioned PSC girder bridges to investigate the effect of short-term prestress losses on the PF distribution. Based on the study results, the following conclusions can be drawn:

1. The variation in PF distribution during tensioning and anchoring was analyzed using the developed Smart Strands. These PF distributions were affected by the short-term prestress losses in the order of friction loss, anchorage seating loss, and elastic shortening loss. They were compared with the theoretical distribution calculated using the predictive equations for the short-term prestress losses. The shape of the PF distributions measured during tensioning does not match the theoretical result that can be mathematically derived considering the friction. This may be due to the unexpected local wobble of a duct and the inevitable entanglement of some strands when inserting into a duct and jacking. In addition, the trend of the anchorage slip and the magnitude of the elastic shortening loss differed from the theoretical values especially in actual bridges. This aspect suggested that the PF distribution in real PSC structures can be more complicated than that realized in ideal conditions of test specimens. However, overall trend of the measured and theoretical PF distributions was similar in each stage of the short-term prestress losses, although the absolute values did differ. These study results revealed that the existing predictive equations for the short-term prestress losses can be useful in estimating the PF distribution for design purposes.

2. The draw-in slip usually ranges from 3 to 6 mm depending on various factors and characteristics of the anchorage device. The assumption on the magnitude of the slip strongly affects the PF distribution. A new methodology was proposed in this study, where the PF distributions measured using Smart Strands were utilized to validate the slip. The pro-

cedure adopted the principle that the area between two PF distributions before and after the anchorage slip divided by the axial stiffness of the strand corresponds to the slip. As a result, the average slip was 5.6 mm in both the full-scale specimen and actual bridges, although the values in the bridges showed more deviation than those in the specimen, which validated the general assumption of 6 mm in slip. The assumption of slip less than 4 mm is so unconservative that it may lead to overestimation of PF.

3. The measured elastic shortening loss showed a relatively larger discrepancy with the theoretical one than the other short-term losses in this study. Therefore, we applied certain strategies in an attempt to reduce this discrepancy. Among several assumptions implied in the predictive equations for the elastic shortening loss that we examined, a few were found to be inevitable for practical purposes, such as a perfect bond between the strand and surrounding concrete. Two possible approaches were attempted in this study. First, using the net section with the duct area deducted instead of a practical gross section increased the elastic shortening loss by 2.7~17.6%. Second, the alternative formulas for the modulus of elasticity of concrete in ACI 318 and Eurocode 2 were attempted in addition to that in a Korean code originally adopted, which changed the modulus of elasticity and the elastic shortening loss by 6.5~19.2%. However, it was difficult to determine which strategy is more effective, because the measured elastic shortening loss remained much larger than the theoretical one even after the improvement made in this study.

4. It is expected that the Smart Strands can be a practical solution for the reasonable assessment of PSC structures, including structural health monitoring during maintenance. In a further study, interpolation of the PF values measured at point sensors such as FBGs can be improved by applying distributed fiber optic sensors, which can realize an almost continuous and smooth profile of the PF distribution. It is also possible to enhance the measurement accuracy by considering the strain transfer effect that inevitably occurs due to the packaging of the fiber optic sensors.

Authors' contributions
SHK designed, performed, and analyzed the experiments, and wrote the paper. SYP and STK provided the Smart Strands and measured the data. SJJ supervised this project as a principal investigator and reviewed the paper. All authors read and approved the final manuscript.

Authors' information

SHK is an Associate Research Engineer in Convergence Technology Research Team, Daewoo Institute of Construction Technology, Korea. He received his BS, MS, and PhD in civil engineering from Ajou University, Korea. SYP is a Research Fellow in Department of Structural Engineering Research, Korea Institute of Civil Engineering and Building Technology, Korea. He received his BS, MS, and PhD in civil engineering from Seoul National University, Korea. STK is a Senior Researcher in Department of Structural Engineering Research, Korea Institute of Civil Engineering and Building Technology, Korea. He received his BS and MS in civil engineering from Kookmin University, Korea. SJJ is a Professor in Department of Civil Systems Engineering, Ajou University, Korea. He received his BS, MS, and PhD in civil engineering from Seoul National University, Korea.

Declarations

Ethics approval and consent to participate
Not applicable.

Consent for publication
Not applicable.

Competing interests
The authors declare that they have no competing interests.

Availability of data and materials
Not applicable.

Author details
[1]Convergence Technology Research Team, Daewoo Institute of Construction Technology, 170, Eulji-ro, Jung-gu, Seoul 04548, Korea. [2]Department of Structural Engineering Research, Korea Institute of Civil Engineering and Building Technology, 283, Goyang-daero, Ilsanseo-gu, Goyang-si 10223, Gyeonggi-do, Korea. [3]Department of Civil Systems Engineering, Ajou University, 206, Worldcup-ro, Yeongtong-gu, Suwon-si 16499, Gyeonggi-do, Korea.

References

Abdel-Jaber, H., & Glisic, B. (2019). Monitoring of long-term prestress losses in prestressed concrete structures using fiber optic sensors. *Structural Health Monitoring, 18*(1), 254–269. https://doi.org/10.1177/1475921717751870

ACI Committee 318. (2019). *Building code requirements for structural concrete (ACI 318–19)*. Farmington Hills: American Concrete Institute (ACI).

American Association of State Highway and Transportation Officials (AASHTO). (2020). *AASHTO LRFD bridge design specifications* (9th ed.). Washington, D.C.: AASHTO

American Society for Testing and Materials (ASTM). (2018). *Standard specification for low-relaxation, seven-wire strand for prestressed concrete (ASTM A416/A416M-18)*. West Conshohocken: ASTM International.

Burns, N. H., Helwig, T., & Tsujimoto, T. (1991). Effective prestress force in continuous post-tensioned beams with unbonded tendons. *ACI Structural Journal, 88*(1), 84–90. https://doi.org/10.14359/2780

Chaki, S., & Bourse, G. (2009). Stress level measurement in prestressed steel strands using acoustoelastic effect. *Experimental Mechanics, 49*, 673–681. https://doi.org/10.1007/s11340-008-9174-9

Cho, K. H., Park, S. Y., Cho, J. R., Kim, S. T., & Park, Y. H. (2015). Estimation of prestress force distribution in the multi-strand system of prestressed concrete structures. *Sensors, 15*(6), 14079–14092. https://doi.org/10.3390/s150614079

European Committee for Standardization (CEN). (2004). *Eurocode 2: Design of concrete structures—Part 1–1: General rules and rules for buildings (EN 1992-1-1)*. Brussels: CEN

Gao, J., Shi, B., Zhang, W., & Zhu, H. (2006). Monitoring the stress of the post-tensioning cable using fiber optic distributed strain sensor. *Measurement, 39*(5), 420–428. https://doi.org/10.1016/j.measurement.2005.12.002

Garber, D. B., Gallardo, J. M., Deschenes, D. J., & Bayrak, O. (2015). Experimental investigation of prestress losses in full-scale bridge girders. *ACI Structural Journal, 112*(5), 553–564. https://doi.org/10.14359/51687909

Jeon, S. J., Park, S. Y., Kim, S. H., Kim, S. T., & Park, Y. H. (2015). Estimation of friction coefficient using Smart Strand. *International Journal of Concrete Structures and Materials, 9*(3), 369–379. https://doi.org/10.1007/s40069-015-0112-9

Jeon, S. J., Shin, H., Kim, S. H., Park, S. Y., & Yang, J. M. (2019). Transfer lengths in pretensioned concrete measured using various sensing technologies. *International Journal of Concrete Structures and Materials, 13*(6), 739–754. https://doi.org/10.1186/s40069-019-0355-y

Joint ACI-ASCE Committee 423. (2016). *Guide to estimating prestress loss (ACI 423.10R-16)*. Farmington Hills: American Concrete Institute (ACI)

Kim, J. M., Kim, H. W., Park, Y. H., Yang, I. H., & Kim, Y. S. (2012). FBG sensors encapsulated into 7-wire steel strand for tension monitoring of a prestressing tendon. *Advances in Structural Engineering, 15*(6), 907–917. https://doi.org/10.1260/1369-4332.15.6.907

Kim, S. H., Park, S. Y., & Jeon, S. J. (2020). Long-term characteristics of prestressing force in post-tensioned structures measured using Smart Strands. *Applied Sciences, 10*(12), 4084. https://doi.org/10.3390/app10124084

Kim, S. T., Park, Y. H., Park, S. Y., Cho, K. H., & Cho, J. R. (2015). A sensor-type PC strand with an embedded FBG sensor for monitoring prestress forces. *Sensors, 15*(1), 1060–1070. https://doi.org/10.3390/s150101060

Kim, S. H., Park, S. Y., Park, Y. H., & Jeon, S. J. (2019). Friction characteristics of post-tensioning tendons in full-scale structures. *Engineering Structures, 183*, 389–397. https://doi.org/10.1016/j.engstruct.2019.01.026

Kim, J. T., Yun, C. B., Ryu, Y. S., & Cho, H. M. (2004). Identification of prestress-loss in PSC beams using modal information. *Structural Engineering and Mechanics, 17*(3–4), 467–482. https://doi.org/10.12989/sem.2004.17.3_4.467

Korea Concrete Institute (KCI). (2012). *Structural concrete design code*. Seoul: KCI.

Lan, C., Zhou, Z., & Ou, J. (2014). Monitoring of structural prestress loss in RC beams by inner distributed Brillouin and fiber Bragg grating sensors on a single optical fiber. *Structural Control and Health Monitoring, 21*(3), 317–330. https://doi.org/10.1002/stc.1563

Lundqvist, P., & Nilsson, L. O. (2011). Evaluation of prestress losses in nuclear reactor containments. *Nuclear Engineering and Design, 241*(1), 168–176. https://doi.org/10.1016/j.nucengdes.2010.11.007

Majumder, M., Gangopadhyay, T. K., Chakraborty, A. K., Dasgupta, K., & Bhattacharya, D. K. (2008). Fibre Bragg gratings in structural health monitoring—Present status and applications. *Sensors and Actuators A: Physical, 147*(1), 150–164. https://doi.org/10.1016/j.sna.2008.04.008

Mehta, P. K., & Monteiro, P. J. M. (2006). *Concrete: Microstructure, properties, and materials* (3rd ed.). New York: McGraw-Hill Companies Inc.

Nellen, P. M., Frank, A., Broennimann, R., Meier, U., & Sennhauser, U. J. (1999). Fiber optical Bragg grating sensors embedded in CFRP wires. *SPIE Proceedings, 3670*, 440–449. https://doi.org/10.1117/12.349758

Neville, A. M. (1996). *Properties of concrete* (4th ed.). Hoboken: John Wiley & Sons Inc.

Nilson, A. H. (1987). *Design of prestressed concrete* (2nd ed.). Hoboken: John Wiley & Sons Inc.

Perry, M., Yan, Z., Sun, Z., Zhang, L., Niewczas, P., & Johnston, M. (2014). High stress monitoring of prestressing tendons in nuclear concrete vessels using fibre-optic sensors. *Nuclear Engineering and Design, 268*, 35–40. https://doi.org/10.1016/j.nucengdes.2013.12.038

Post-Tensioning Institute (PTI). (2006). *Post-tensioning manual* (6th ed.). Phoenix: PTI

Rodrigues, C., Félix, C., Lage, A., & Figueiras, J. (2010). Development of a long-term monitoring system based on FBG sensors applied to concrete bridges. *Engineering Structures, 32*(8), 1993–2002. https://doi.org/10.1016/j.engstruct.2010.02.033

Shen, S., Wang, Y., Ma, S. L., Huang, D., Wu, Z. H., & Guo, X. (2018). Evaluation of prestress loss distribution during pre-tensioning and post-tensioning using long-gauge fiber Bragg grating sensors. *Sensors, 18*(12), 4106. https://doi.org/10.3390/s18124106

Tan, X., Bao, Y., Zhang, Q., Nassif, H., & Chen, G. (2021). Strain transfer effect in distributed fiber optic sensors under an arbitrary field. *Automation in Construction, 124*, 103597. https://doi.org/10.1016/j.autcon.2021.103597

VSL International Ltd. (2015). *VSL strand post-tensioning systems*. Koniz: VSL International Ltd.

Washer, G. A., Green, R. E., & Pond, R. B., Jr. (2002). Velocity constants for ultrasonic stress measurement in prestressing tendons. *Research in Nondestructive Evaluation, 14*, 81–94. https://doi.org/10.1007/s00164-002-0003-8

Yao, Y., Yan, M., & Bao, Y. (2021). Measurement of cable forces for automated monitoring of engineering structures using fiber optic sensors: A review. *Automation in Construction, 126*, 103687. https://doi.org/10.1016/j.autcon.2021.103687

Publisher's Note